Highly Damping and Self-Healable Ionic Elastomer from Dynamic Phase Separation of Sticky Fluorinated Polymers

Huai Xiang, Xiaoxia Li, Baohu Wu, Shengtong Sun, and Peiyi Wu**

Shock-induced low-frequency vibration damage is extremely harmful to bionic soft robots and machines that may incur the malfunction of fragile electronic elements. However, current skin-like self-healable ionic elastomers as the artificial sensing and protecting layer still lack the ability to dampen vibrations, due to their almost opposite design for molecular frictions to material's elasticity. Inspired by the two-phase structure of adipose tissue (the natural damping skin layer), here, a highly damping ionic elastomer with energy-dissipating nanophases embedded in an elastic matrix is introduced, which is formed by polymerization-induced dynamic phase separation of sticky fluorinated copolymers in the presence of lithium salts. Such a supramolecular design decouples the elastic and damping functions into two distinct phases, and thus reconciles a few intriguing properties including ionic conductivity, high stretchability, softness, strain-stiffening, elastic recovery, room-temperature self-healability, recyclability, and most importantly, record-high damping capacity at the human motion frequency range (loss factor tan $\delta > 1$ at 0.1–50 Hz). This study opens the door for the artificial syntheses of high-performance damping ionic skins with robust sensing and protective applications in soft electronics and robotics.

1. Introduction

Human skin with the unparalleled combination of elasticity, ionic perception, and wound self-repairing properties has inspired the artificial syntheses of numerous self-healing ionic elastomers for advanced sensing applications with extended service life.[1] These ionic elastomers, also known as ionic skins, can not only adhere on human skin for motion or electrophysiology monitoring, but also adapt to soft robots and machines as the sensing and protecting layer to fully replicate human skin's functions.[2,3] While self-healability and ionic conduction are easily imparted via designing ion-involving supramolecular polymer networks, the resistance of ionic skins to various damages is considered to be a quite challenging task without sacrificing the other properties. Noteworthily, human-like bionic soft robots may be frequently exposed to sudden shocks, strikes, or mechanical agitations with low-frequency vibrations (0.1–50 Hz), which will likely incur the malfunction or fatigue failure of internal fragile electronic elements.[4,5] Despite the recent progress in toughening self-healable ionic skins by supramolecular networks, phase separations, or hard domains to resist global and crack-related damages,[6–9] rare reports focus on improving its mechanical damping performance to isolate or eliminate the equally important shock-induced vibration damages.

Damping generally describes the attenuation of unwanted vibrations by dissipating shock-related mechanical energy into heat by means of spatial momentum transfer driven by velocity gradient.[10] For elastomers, manipulating polymer viscoelasticity to enhance internal molecular frictions is considered to be the key to improving damping capacity.[11,12] In principle, when the time scales of viscoelastic relaxation and vibration are comparable (i.e., the ratio of relaxation time to vibration time defined as Deborah number, D_e, is approximate to 1), maximum damping can be realized.[5,13] Unfortunately, most elastomers are poorly damping with a rather low loss factor (tan $\delta < 0.1$) which is defined by the ratio (G''/G') of the loss (G'') to storage moduli (G'). Optimizing the associating dynamics of polymer networks to the gel point can afford very high tan δ values close to 1, yet the elasticity and shape retention of the resulting materials are pretty low.[14–16] Shifting or broadening the glass transition region with an apparent tan δ peak to the working temperature/frequency range has been widely utilized to optimize elastomer's damping performance by copolymerization,[17] polymer blending,[18] interpenetrating network,[5,19] incorporating granules,[20] metal coordination,[21] dynamic networks,[22] etc. However, materials at the glass transition region have often limited stretchability and elastic recovery, and the relatively high moduli also hamper ionic skin-related applications in soft electronics and robotics. Alternatively, introducing additional relaxation components such as dangling chains,[13,23] polymer fluids,[12] and nematic liquid crystal orders[24] into an elastic network has been recently reported to produce highly

H. Xiang, X. Li, S. Sun, P. Wu
State Key Laboratory for Modification of Chemical Fibers and Polymer Materials
College of Chemistry and Chemical Engineering & Center for Advanced Low-dimension Materials
Donghua University
2999 North Renmin Road, Shanghai 201620, China
E-mail: shengtongsun@dhu.edu.cn; wupeiyi@dhu.edu.cn

B. Wu
Jülich Centre for Neutron Science (JCNS) at Heinz Maier-Leibnitz Zentrum (MLZ) Forschungszentrum Jülich
Lichtenbergstr. 1, 85748 Garching, Germany

damping elastomers without recalling glass transition. Nevertheless, the premised permanent network for constraining the random reptation of dissipating chains hinders efficient self-healability. To the best of our knowledge, none of the previous strategies can synergize damping, elasticity, and self-healability in one elastomer to meet the shock-resistant requirements of ionic skins.

It is noticed that human skin is naturally damping for shock attenuation owing to the presence of subcutaneous adipose tissues throughout the body, in which adipocytes form lobules surrounded by an elastic extracellular matrix (ECM) (**Figure 1**a).[25] The loosely connected ECM shapes the soft adipose tissue (Young's modulus ≈ 1 kPa) that experiences even larger strains than dermis, while adipocytes are filled with viscous lipids (molecular weight ≈ 900 g mol^{-1}; viscosity ≈ 36.8 mPa s at 37 °C) as the dissipating elements, together contributing to both high elasticity and damping capacity (tan $\delta \approx 0.3$–0.4) of the whole adipose layer.[26–28] Such a heterogeneous two-phase structure of adipose tissue comprising of elastic matrix and dissipating cells represents a totally different damping-but-elastic mechanism from all the above-mentioned strategies. In addition, with the aid of fibroblasts, adipose tissues can also self-repair wounds by fully restoring the mechanical and ionic sensing properties. Thus, we envision that the combined elastic, damping, and self-healable properties of ionic elastomers may be simultaneously realized if an adipose tissue-like phase-separated structure can be formed within a supramolecular ion-conducting matrix.

Herein, inspired by adipose tissue's heterogenous structure, we report the first example of highly damping and self-healable ionic elastomer from the dynamic phase separation of sticky fluorinated polymers. As illustrated in Figure 1b, the dynamic phase separation is in situ induced by the one-step

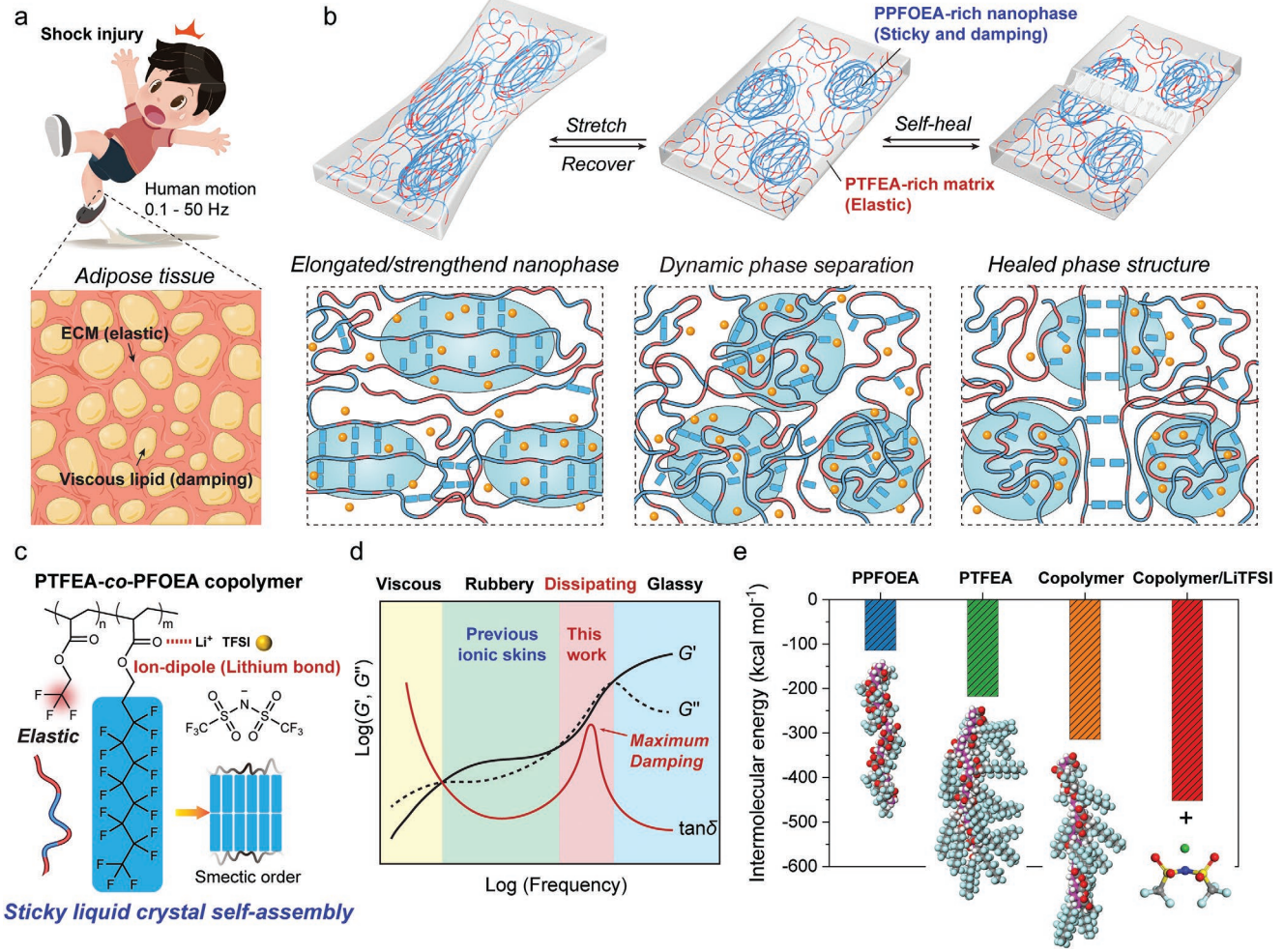

Figure 1. a) Schematic shock-induced low-frequency vibration injuries to a moving human body and the unique elastic-but-damping two-phase structure of adipose tissue for skin protection. b) Adipose tissue-inspired design of highly damping ionic elastomer from the dynamic phase separation of sticky fluorinated copolymers. In the ionic elastomer, PTFEA-rich matrix is highly entangled contributing to elasticity, while liquid-like PPFOEA-rich nanophases are highly dissipating with short-range smectic liquid crystal order contributing to damping capacity. Upon stretch, the PPFOEA-rich nanophases are deformable accompanied by strain-enhanced liquid crystal assembly. The ionic elastomer also readily self-heals at room temperature from the reconstruction of supramolecular structure. c) Chemical structure of PTFEA-*co*-PFOEA/LiTFSI with denoted smectic liquid crystal self-assembly and lithium bond. d) Typical rheology of viscoelastic polymers. Previous ionic skins were mainly designed to work at the rubbery regime, while the present ionic elastomer works at the dissipation regime with a maximum damping peak at the human motion frequency range (0.1–50 Hz). e) Intermolecular energies of PTFEA, PPFOEA, PTFEA-*co*-PFOEA, and PTFEA-*co*-PFOEA/LiTFSI calculated by molecular dynamics simulation.

copolymerization of two distinct fluorinated monomers with short (TFEA: 2,2,2-trifluoroethyl acrylate) and long side chains (PFOEA: 2-perfluorooctylethyl acrylate), respectively, which features highly dissipating PPFOEA-rich nanophases embedded in a highly entangled PTFEA-rich matrix. Between them, TFEA moieties are flexible and freely entangled contributing to elasticity, while sticky PFOEA moieties tend to form transient liquid crystal self-assemblies contributing to strong interchain frictions and high damping capacity. Analogous to adipose tissue, such a dynamic phase separation well decouples elastic and damping functions into two phases, and thus defeats the long-term conflict among elasticity, damping, and self-healability for viscoelastic polymers. At room temperature (20 °C), the optimal copolymer ionic elastomer with equimolar TFEA and PFOEA can reach superhigh stretchability (2168% elongation), softness (modulus ≈1.0 MPa), strain-adaptive stiffening, good elastic recovery (87% instant recovery from 1,500% strain), full self-healability, recyclability, as well as ultrahigh loss factors at the human motion frequency range (tan $\delta > 1$ at 0.1–50 Hz). We further demonstrate the energy-dissipating and damping performance of the ionic elastomer in tension, compression, and vibration modes, which shows promising applications as shock-resistant robust ionic skin in soft electronics and robotics.

2. Results and Discussion

To mimic adipose tissue's phase-separated structure, it is the key to choosing suitable supramolecular systems with not only adjustable associating dynamics for proper control over molecular frictions, but also apparent phase immiscibility to decouple elastic and damping functions. Sticky or associative polymers are a class of promising supramolecular systems composed of linear polymers transiently cross-linked through the multiple breaking and reforming of reversible non-covalent bonds as effective friction centers.[29] Importantly, it is easy to tailor the rheological properties of sticky polymers by changing the type and content of associative groups, which are also termed "stickers". In this work, we carefully selected fluorinated acrylate copolymer as the candidate sticky polymer, since its molecular aggregation structure is highly dependent on side chain length. Short-side-chain poly(fluoroalkyl acrylate)s like PTFEA are amorphous and rubbery with lower glass transition temperatures than room temperature (for PTFEA, $T_g \approx -10$ °C). However, when fluoromethylene number ≥8 (e.g., PPFOEA), the increased chemical incompatibility between fluorinated pendent groups and hydrocarbon backbone forces the bulky rigid-rod-like side chains to self-organize into an ordered head-to-head lamellar structure, which is called smectic liquid crystal phase (Figure 1c).[30–32] Copolymerizing PFOEA with amorphous monomers can partially break the structural order of liquid crystal assemblies, thus allowing for the wide tunability of interchain frictions.[33] Moreover, the distinct aggregation behavior and fluorinated contents of PTFEA and PPFOEA make the phase separation of PTFEA-*co*-PFOEA easily occur, and thus enable the decoupling of elastic and damping functions into two different phases. Therefore, by balancing the ratio of PTFEA-rich elastic and PPFOEA-rich dissipating components, good elastic recovery, high damping, and self-healability can be simultaneously realized.

It is highlighted that, different from the phase separations of other sticky copolymer elastomers forming solid-like hard nanodomains,[34–36] the phase separation of PTFEA-*co*-PFOEA is highly dynamic involving liquid-like nanodomains. This is essential because only the dissipating regime (or glass transition region) in the typical frequency-dependent rheological curves of viscoelastic polymers can afford maximum damping capacities featuring both a tan δ peak and high loss moduli (Figure 1d). In this regime, the peak value of tan δ even exceeds 1, which was previously ascribed to a "liquid–liquid" transition by Boyer related to the disruption of short-range order.[37] Accordingly, the PPFOEA-rich liquid-like nanodomains are highly deformable and even grow in size during stretch caused by strain-enhanced liquid crystal assembly, imparting the ionic elastomer with high damping performance and rapid self-healability (Figure 1b). On the other hand, entropic elastic recovery is ensured by the highly entangled PTFEA-rich matrix, which locates at the rubbery regime. In contrast, most of previous ionic skins possessing either chemical or physical cross-links were designed to work only in the rubbery regime that might have high elasticity but rather low damping capacities at normal motion frequencies (Figure 1d).[6,38–42]

To support the design rationale of PTFEA-*co*-PFOEA ionic elastomer, we employed molecular dynamics simulation to calculate the intermolecular energies of different polymers that are directly related to their internal molecular frictions (Figure S1, Supporting Information). As presented in Figure 1e, although PFOEA moieties tend to self-assemble into ordered structures, in PPFOEA homopolymer, the large steric hindrance of rigid fluorinated side chains does not allow for close packing among different chains, resulting in an even lower intermolecular energy than amorphous PTFEA homopolymer. However, in PTFEA-*co*-PFOEA copolymer, the involved TFEA moieties as chain spacers can efficiently accommodate the close packing among adjacent PFOEA side chains and thus facilitate strong interchain association, resulting in a much higher intermolecular energy. Introducing lithium bis(trifluoromethanesulfonyl) imide (LiTFSI) as the conducting medium would further physically cross-link carbonyl groups by $Li^+ \cdots O{=}C$ ion-dipole interactions (also called lithium bonds in other papers;[43,44] Figure 1c), leading to even stronger intermolecular interactions as well as thermal stability. The simulation results suggest that by copolymerizing TFEA and PFOEA in proper ratios to balance the associating dynamics and molecular frictions, high damping capacity shall be successfully endowed to the phase-separated ionic elastomer.

Experimentally, PTFEA-*co*-PFOEA ionic elastomers were prepared by one-step photo-induced copolymerization of TFEA and PFOEA in the presence of 1 M LiTFSI. A small amount of ionic liquid (5 mol% with respect to total monomer), EMI TFSI (EMI: 1-ethyl-3-methylimidazolium), was also introduced to promote ionic conduction; however, higher amounts of EMI TFSI than 5 mol% could not be well dissolved in the polymer due to its poor compatibility with fluorinated chains (Figure S2, Supporting Information). We carefully varied the molar contents of PFOEA to search for the optimum ionic elastomer with all the balanced properties. Notably, neat PTFEA and PTFEA-*co*-PFOEA

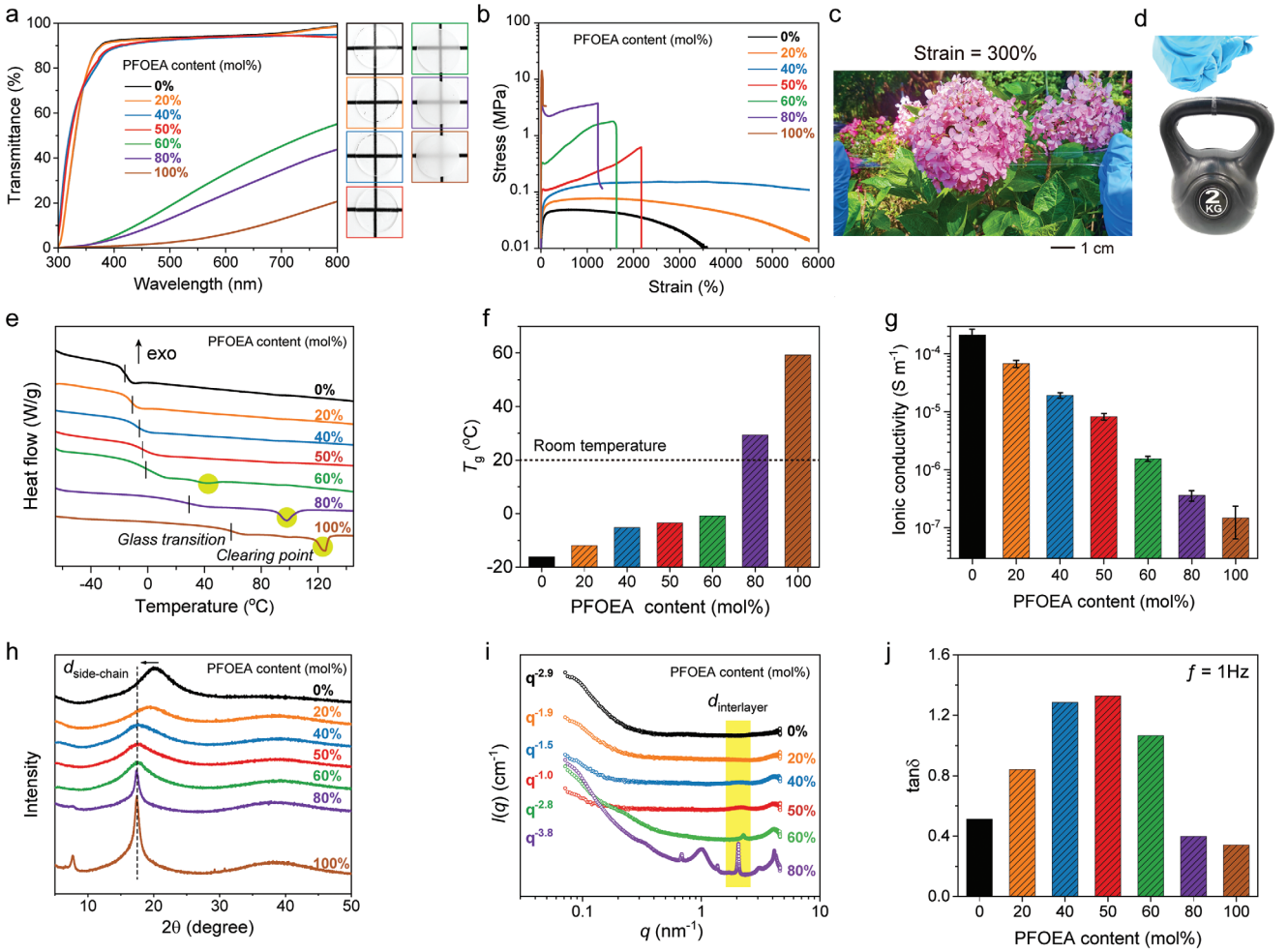

Figure 2. a) Photos and visible transmittance spectra of PTFEA-*co*-PFOEA/LiTFSI with different PFOEA contents. b) Nominal tensile stress-strain curves (strain rate: 0.08 s^{-1}). c) A stretched PTFEA-*co*-$PFOEA_{50\%}$ ionic elastomer film to 300% strain. d) A 2-g-weight PTFEA-*co*-$PFOEA_{50\%}$ ionic elastomer film can lift up a 2-kg-weight load without breaking. e) DSC heating curves with labelled glass transitions and clearing points. f,g) PFOEA content-dependent glass transition temperatures and ionic conductivities. The error bars represent ±SD from the mean value (n = 3). h,i) XRD and SAXS profiles of PTFEA-*co*-PFOEA/LiTFSI with different PFOEA contents. The characteristic peaks for side-chain and interlayer distances are labeled. j) PFOEA content-dependent tan δ values measured at 1 Hz.

ionic elastomers with PFOEA molar contents less than 50 mol% are optically transparent with ≈90% transmittance in the visible range (**Figure 2**a). By further increasing PFOEA contents (60, 80, and 100 mol%), the copolymers became noticeably opaque, indicating the emergence of macroscopic phase separation due to the formation of ordered PPFOEA smectic structure. This was evidenced by polarized optical microscope (POM) observations (Figure S3, Supporting Information), in which no birefringence was observed for all the ionic elastomers with PFOEA contents <50 mol% corresponding to an amorphous structure, while strong liquid crystal birefringence was observed in the cases of higher PFOEA contents (60–100 mol%).

PFOEA contents also greatly affect the mechanical properties of the resulting materials. The calculated Young's moduli from tensile stress–strain curves increased with increasing PFOEA contents, which validates the gradual enhancement of PFOEA-related interchain associations (Figure 2b; Figure S4, Supporting Information). Notably, the ionic elastomers with 0, 20, and 40 mol% PFOEA are highly stretchable with maximum elongations >3,500% (not break), and strain softening with stress declination took place at higher strains. Strain softening generally arises from the irreversible chain sliding that cannot be recovered in the subsequent releasing process. In contrast, the ionic elastomer with 50 mol% PFOEA (i.e., equimolar TFEA and PFOEA; denoted as PTFEA-*co*-$PFOEA_{50\%}$) is not only highly stretchable with a maximum elongation of 2,168%, but also strain-adaptive stiffening. Converted true stress–strain curve (Figure S5, Supporting Information) showed first a short strain-softening process from the initial modulus of 1.0 MPa at 0% strain to 0.1 MPa at 40% strain following the classical affine deformation prediction;[37] after that, the ionic elastomer rapidly stiffened in the following strains to a final modulus of 2.4 MPa at 2168% strain. It should be mentioned that, strain-stiffening is a valuable mechanical property for all the skin-mimetic materials, which represents a key self-protective mechanism of human skin to prevent injury upon malicious stretch.[8] We here ascribe the skin-like strain-stiffening response of

PTFEA-*co*-PFOEA$_{50\%}$ ionic elastomer to the strain-enhanced liquid crystal assembly of PFOEA moieties as illustrated in Figure 1b (mechanism will be discussed later). After stretching to 300% strain, the PTFEA-*co*-PFOEA$_{50\%}$ ionic elastomer remained highly transparent (Figure 2c). In situ POM observations of the stretching process revealed very homogenous structural orientation of ionic elastomer along the stretching direction (Figure S6, Supporting Information). The calculated toughness from the nominal stress–strain curve is 5.4 MJ m^{-3}, high enough to lift a load ≈1,000 times heavier than the ionic elastomer itself (Figure 2d). By further increasing PFOEA contents to 60, 80, and 100 mol%, apparent yielding was observed due to PFOEA smectic ordering, and these samples can be no longer recognized as elastomers. Without flexible TFEA spacers to accommodate PFOEA assemblies, neat PPFOEA/LiTFSI is stiff yet brittle.

Glass transition is crucial to PTFEA-*co*-PFOEA ionic elastomer, at which the maximum energy dissipation of PPFOEA-rich nanophases takes place. As shown in the differential scanning calorimetry (DSC) curves (Figure 2e,f), with increasing PFOEA contents, T_g gradually increased. There was only one glass transition event detected for all the copolymers, demonstrating that TFEA and PFOEA were indeed randomly copolymerized with approximate reactivities. Moreover, the T_gs of the ionic elastomers with PFOEA contents <60 mol% are all lower than room temperature (20 °C), implying their chain flexibility for rubbery appearance. However, the smectic structure of PTFEA-*co*-PFOEA$_{60\%}$ as evidenced by the emergence of clearing point (see temperature-dependent POM images in Figure S7, Supporting Information) made it deformed as a plastic, and so did the copolymers with even higher PFOEA contents. It is also noted that the clearing point (125 °C) of PPFOEA/LiTFSI is much higher than pure PPFOEA (74 °C),[32] suggesting that lithium bond-mediated physical cross-linking is predominant in PPFOEA domains. Copolymerizing with TFEA shifted the clearing point of PPFOEA to lower temperatures (98 °C for 80 mol% PFOEA and 42 °C for 60 mol% PFOEA), consolidating the role of TFEA moieties as flexible spacers in weakening PFOEA assemblies.[45] As shown in Figure 2g, the ionic conductivities of PTFEA-*co*-PFOEA/LiTFSI followed an inverse order to glass transition temperatures. This is reasonable because ion conduction strongly depends on chain mobility. While the chain flexibility in the cases of PFOEA contents lower than 60 mol% provided acceptable ionic conductivities (>10^{-6} S m^{-1}), glass transition- and liquid crystallization-induced chain freezing events in the cases of 80 and 100 mol% PFEOA led to relatively small ionic conductivities (<2×10^{-7} S m^{-1}).

Powder X-ray diffraction (XRD) was also performed to elucidate the structural evolution of PTFEA-*co*-PFOEA/LiTFSI with varied PFOEA contents. As shown in Figure 2h, the remarkable peak at $2\theta \approx 18°$ corresponds to the average distance among fluorinated side chains ($d_{\text{side-chain}}$).[32] For PPFOEA/LiTFSI, the $d_{\text{side-chain}}$ of 0.51 nm calculated from the sharp liquid crystalline peak is characteristic for the hexagonal in-plane lattice constant of smectic phase.[33] PTFEA with a smaller side chain volume has also a smaller $d_{\text{side-chain}}$ than PPFOEA. With increasing PFOEA contents, $d_{\text{side-chain}}$ first increased significantly from 0.44 nm for pure PTFEA/LiTFSI to 0.51 nm for PTFEA-*co*-PFOEA$_{50\%}$/LiTFSI, and then remained unchanged at higher PFOEA contents (Figure S8, Supporting Information). This again indicates that, as PFOEA content exceeds 50 mol%, the close packing of PFOEA moieties into smectic phase becomes possible resulting in plastic-like polymers. A similar trend was also observed in the spin–spin relaxation time (T_2) changes of low-field ^{19}F NMR spectra that reflected the mobility of fluorinated side chains (Figure S9, Supporting Information).

Small-angle X-ray scattering (SAXS) was further employed to investigate the structural changes at the nanoscale. SAXS intensities (I) were plotted against scattering vector (q) in log–log scale as a function of PFOEA contents (Figure 2i). In the q regime larger than 0.2 nm^{-1}, the scattering curves showed a broad peak around q = 2.2 nm^{-1} (corresponding to an interlayer distance of $d = 2\pi/q$ = 2.9 nm)[33] in the PTFEA-*co*-PFOEA samples with 40 and 50 mol% PFOEA, which reveals the existence of short-range order for PFOEA liquid crystal assemblies. With further increasing PFOEA contents, remarkable liquid crystalline peaks appeared in the scattering profiles along with the disappearance of weak short-range-order peak. The scattering curves in the q regime smaller than 0.2 nm^{-1} showed the existence of phase-separated structures with scales larger than 60 nm, and the characteristic inner structures are strongly dependent on PFOEA contents. In this q regime, the scattering curves were characterized by the power law behavior of the scattering function $I(q) \sim q^n$. The power law exponent (n) increased from −2.9 at 0 mol% to −1.5 at 40 mol% and then reached a maximum value of −1.0 at 50 mol% PFOEA. This reveals that, with increasing PFOEA contents, the inner structure changed from dense bird's nest (n = −2.9), to gauss chain (n = −1.9) and semi-rigid flexible chain network (n = −1.5), and then to rod-like (n = −1.0) at 50 mol% PFOEA. For the samples with PFOEA contents larger than 50%, the power law exponent decreased to −2.8 (60 mol%) and −3.8 (80 mol%) due to the appearance of dense liquid crystal domains. All the above results suggest that PTFEA-*co*-PFOEA$_{50\%}$ ionic elastomer is most loosely packed at the nanoscale, as compared to high chain entanglement in PTFEA/LiTFSI and liquid crystallization in PPFOEA/LiTFSI.

The balanced chain entanglement and transient liquid crystal assembly at 50 mol% PFOEA make PTFEA-*co*-PFOEA$_{50\%}$ ionic elastomer rather special in terms of damping properties. We performed the rheological tests of all the PTFEA-*co*-PFOEA/LiTFSI samples at room temperature (Figure S10, Supporting Information). The G' and G'' relationship at 0.1 Hz was used to determine the rheological state of the sample at the experimental quasi-static time scale.[46] It is clear that neat PTFEA/LiTFSI is in the rubbery state due to chain entanglement, and neat PPFOEA/LiTFSI is in the glassy state due to liquid crystallization. PTFEA-*co*-PFOEA/LiTFSI samples with different PFOEA contents are just between the two neat samples. In particular, a typical dissipation behavior with close G' and G'' was observed for the samples with PFOEA contents between 40 and 60 mol%. Importantly, the loss factor (tan δ), critical for the damping performance, ranked to a maximum of 1.3 at 50 mol% PFOEA at the typical human motion frequency of 1 Hz (Figure 2j), suggesting that PTFEA-*co*-PFOEA$_{50\%}$ ionic elastomer is optimal for shock-resistant ionic skin applications.

Infrared (IR) spectroscopy was additionally used to elucidate the subtle internal interactions of PTFEA-*co*-PFOEA/LiTFSI. In this work, we focused on three spectral regions,

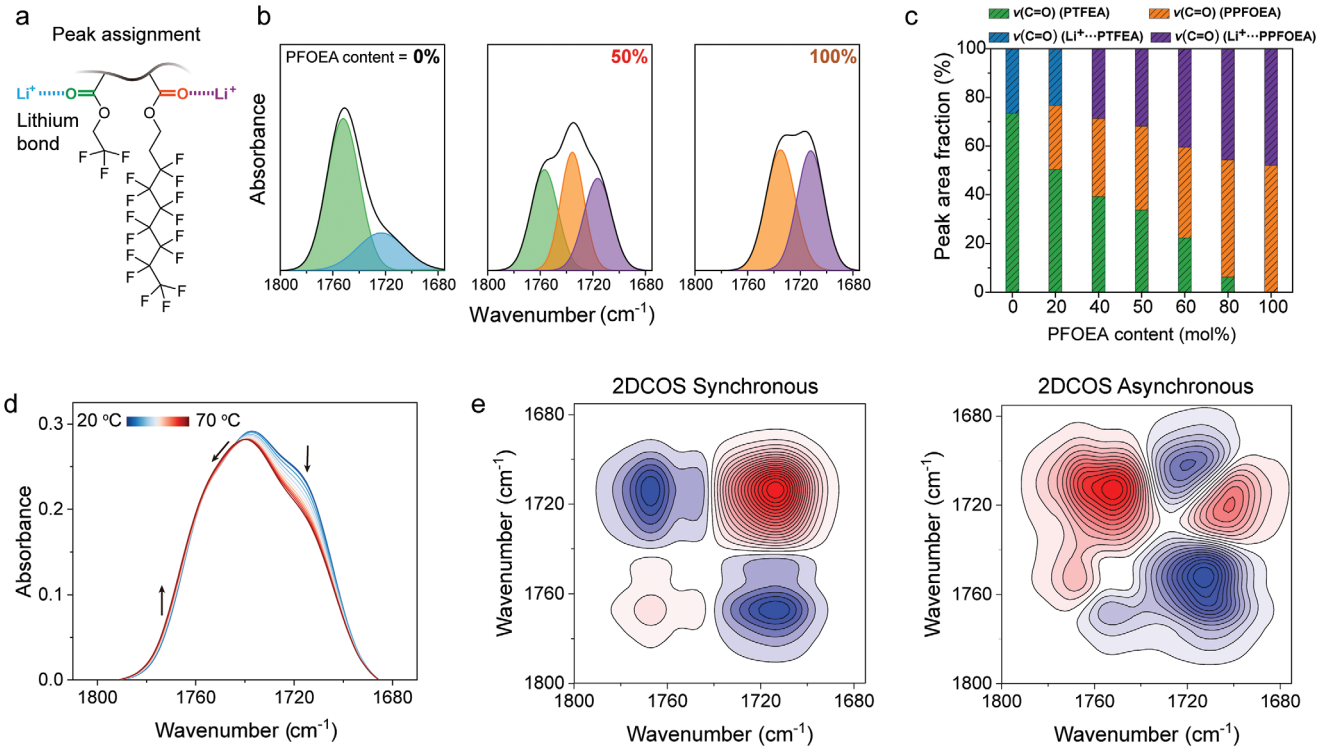

Figure 3. a) Schematic four kinds of C=O groups with/without lithium bonds. b) Curve-fitted ν(C=O) ATR-FTIR spectra of PTFEA-*co*-PFOEA/LiTFSI with 0, 50, and 100 mol% PFOEA contents (see other spectra in Figure S14, Supporting Information). c) Peak area fraction changes of four ν(C=O) peaks as a function of PFOEA contents. d) Temperature-variable transmission IR spectra of PTFEA-*co*-PFOEA$_{50\%}$ ionic elastomer upon heating from 20 to 70 °C (interval: 5 °C). e) 2DCOS synchronous and asynchronous spectra generated from (d). In 2DCOS spectra, red color represents positive intensities, while blue color represents negative intensities.

i.e., C=O stretching (ν(C=O)), C−F asymmetric stretching (ν_{as}(CF$_2$)), and S−N−S asymmetric stretching (ν_{as}(SNS)), to monitor the PFOEA content-dependent changes of polymer backbones, fluorinated side chains, and LiTFSI, respectively. Owing to the presence of lithium bonds, the ν(C=O) peak splits into two to three peaks corresponding to free C=O and lithium bonds with different C=O groups (**Figure 3**a). Notably, the presence of lithium bonds as effective physical cross-links greatly improved the thermal stability of PTFEA-*co*-PFOEA$_{50\%}$ ionic elastomer which remained a solid till 160 °C, while pure PTFEA-*co*-PFOEA$_{50\%}$ elastomer (without LiTFSI) transformed to a viscous liquid at ≈107 °C, supported by the comparison of both temperature-sweep rheological test and low-field ^{19}F NMR spectra (Figures S11 and S12, Supporting Information). Nevertheless, no significant influence of lithium bonds on the liquid crystal assembly of fluorinated side chains was observed (Figure S13, Supporting Information). For clarity, we fitted the ν(C=O) peaks of all the PTFEA-*co*-PFOEA/LiTFSI samples with four main species: 1,752 cm^{-1} (ν(C=O) (PTFEA)), 1,735 cm^{-1} (ν(C=O) (PPFOEA)), 1,723 cm^{-1} (ν(C=O) (Li$^+$···PTFEA)), and 1,712 cm^{-1} (ν(C=O) (Li$^+$···PPFOEA)) (Figure 3b and Figure S14, Supporting Information). The peak area fractions of different samples are plotted in Figure 3c. Interestingly, except for the PFOEA content-dependent regular changes of ν(C=O) peaks for free PTFEA and PPFOEA, ν(C=O) (Li$^+$···PTFEA) was replaced by ν(C=O) (Li$^+$···PPFOEA) at the PFOEA contents larger than 20 mol%. This implies that, the lithium bond in PPFOEA is much stronger than that in PTFEA, and thus in the optimal PTFEA-*co*-PFOEA$_{50\%}$ ionic elastomer, lithium bond-related physical cross-linking mainly functions in the PPFOEA-rich dissipating nanophases, while PTFEA-rich matrix is less interfered. Moreover, with increasing PFOEA contents, the continuous shift of ν_{as}(CF$_2$) (only present in PFOEA side chains) to lower wavenumbers corresponds to the gradually enhanced PFOEA assemblies with stronger dipole-dipole interactions (Figure S15, Supporting Information). Along with the enhanced lithium bonds, ν_{as}(SNS) from TFSI anions first shifts to higher wavenumbers with increasing PFOEA contents, and then to lower wavenumbers at high PFOEA contents, which is ascribed to be promoted by the previously reported "fluorous effect" (Figure S16, Supporting Information).[47,48]

Temperature-variable IR and 2D correlation spectroscopy (2DCOS) were employed to clarify the dominating event in the temperature-related energy dissipation process of PTFEA-*co*-PFOEA$_{50\%}$ ionic elastomer. As shown in Figure 3d, as temperature rose from 20 to 70 °C, the intensity of ν(C=O) (Li$^+$···PPFOEA) peak at 1,712 cm^{-1} drastically decreased suggesting thermal-induced weakening of lithium bonds. In contrast, only slight peak shifts or intensity changes were observed for ν(C=O) (PPFOEA) and ν(C=O) (PTFEA) caused by dipolar interaction changes. 2DCOS was generated from all the temperature-variable IR spectra, which consists of synchronous and asynchronous spectra (Figure 3e). According to Noda's judging rule,[8,49] the sequential order in the heating

process can be determined to be (→ means prior to or earlier than; see operation details in Table S1, Supporting Information): 1,704 cm^{-1} → 1,714 cm^{-1} → 1,735 cm^{-1} → 1,752 cm^{-1}, i.e., ν(C=O) ($Li^+\cdots$PPFOEA) (strong) → ν(C=O) ($Li^+\cdots$PPFOEA) (weak) → ν(C=O) (PPFOEA) → ν(C=O) (PTFEA). Note that, the two new peaks at 1,704 and 1,714 cm^{-1} as discerned by 2DCOS asynchronous spectrum are split from the original peak at 1,712 cm^{-1} in the 1D spectrum, and assigned to strong and weak lithium bonds, respectively. Altogether, the significant spectral variations and earlier events of PFOEA-related lithium bonds clearly reveal the dominating role of PPFOEA-rich sticky chains in the critical energy dissipation process.

All the above investigations demonstrate that, the phase-separated PTFEA-*co*-$PFOEA_{50\%}$ ionic elastomer with balanced chain entanglement and associating dynamics may synergize the combined properties of elasticity, self-healability, and damping capacity (otherwise stated, all the ionic elastomers hereafter are referred to the sample with 50 mol% PFOEA content). We first evaluated the elasticity and energy dissipating properties of the ionic elastomer recovered from large deformations, which are generally involved in various shock-related scenarios.[11] As shown in **Figure 4**a–d, stretching or compressing the ionic elastomer to different strains led to excellent recovery as well as large dissipation in the releasing process. When stretched at a low strain rate of 0.08 s^{-1}, the dissipated energy drastically increased from 43 kJ m^{-3} for 200% strain to 260 kJ m^{-3} for 1,000% strain, while the energy dissipation ratio (defined by the ratio of dissipated energy to stored energy) remained high at 52–65%. A similar trend was also observed in the compressive mode with the dissipated energy ranging from 1.9 to 82 kJ m^{-3} and dissipation ratio ≈78–87% when compressed to 20–80% strains at a strain rate of 0.05 s^{-1}. Increasing stretching and compressing strain rates further increased the dissipated energies and dissipation ratios, in accordance with

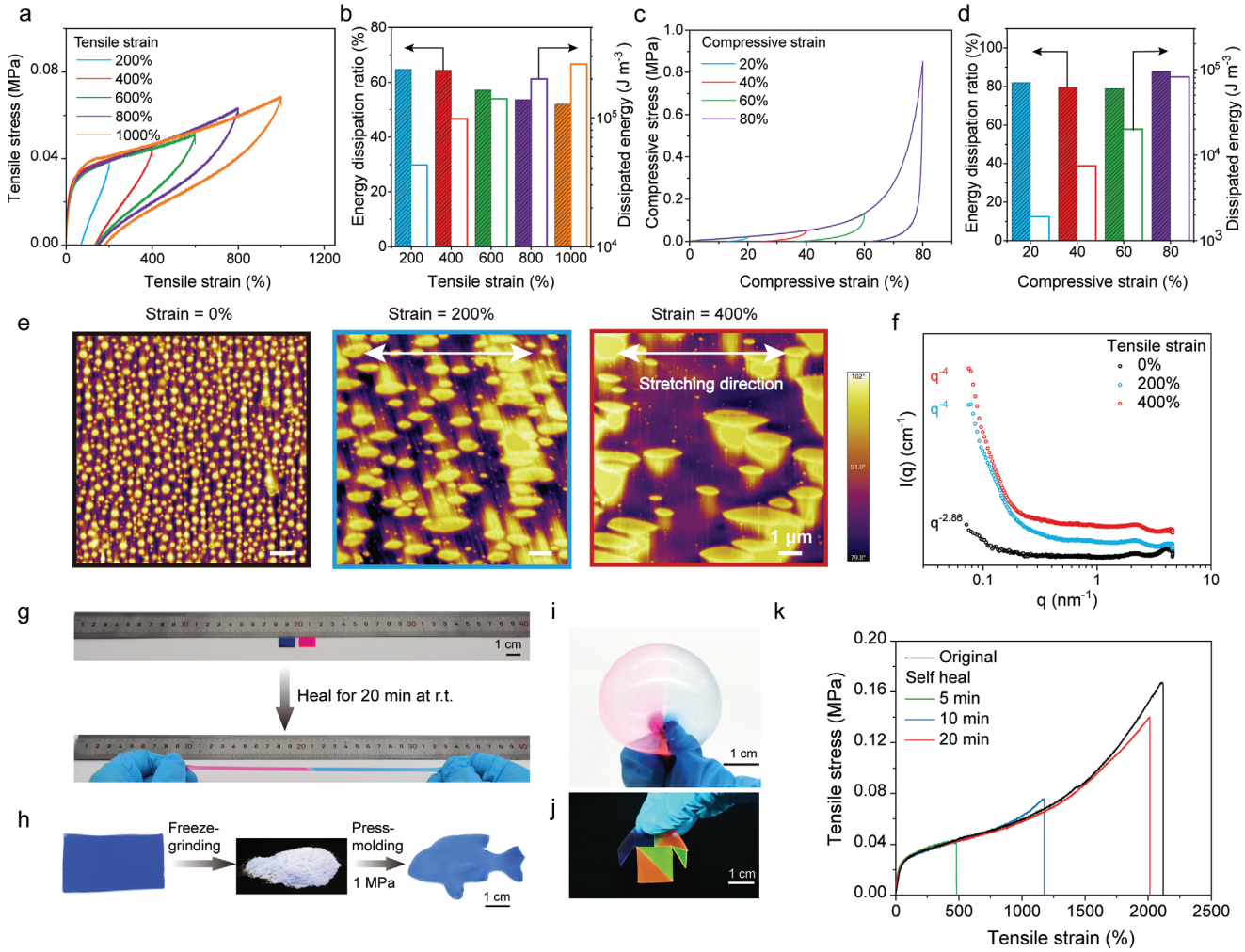

Figure 4. a) Tensile loading-unloading curves of PTFEA-*co*-$PFOEA_{50\%}$ ionic elastomer to/from different strains (strain rate: 0.08 s^{-1}). b) Tensile strain-dependent energy dissipation ratios and dissipated energies. c) Compressive loading–unloading curves to/from different strains (strain rate: 0.05 s^{-1}). d) Compressive strain-dependent energy dissipation ratios and dissipated energies. e) AFM phase images of ionic elastomer as stretched to the strains of 200% and 400%. f) Strain-dependent SAXS curves. g) Two healed ionic elastomer pieces at room temperature for 20 min can be stretched as a whole. h) The ionic elastomer can be recycled and press-molded into any shape from freeze-ground powers. i) The healed ionic elastomer can be blown into an airtight balloon. j) Specific shapes can be obtained by the self-healing process of several ionic elastomer tangram pieces. k) Tensile curves of ionic elastomer healed for different periods at room temperature.

the frequency-induced increase of G″ and tan δ values in the low-frequency range (Figures S17 and S18, Supporting Information). It is noted that the calculated energy dissipation ratios are higher than previously reported highly damping liquid crystalline elastomers and polymer-fluid gels as well as commercial damping elastomers (e.g., Sorbothane®).[12,50,51] This means that the PTFEA-*co*-PFOEA ionic elastomer has the ability to dissipate large deformation energy, important for shock-resistant and impact-protective applications.

After stretching to large strains, the ionic elastomer needed about 2 min for full strain recovery. This actually corresponds to a slow recovery phenomenon arising from the apparent energy dissipating process (Movie S1, Supporting Information), typical for damping elastomers.[24] Without waiting, cyclically stretching the ionic elastomer for 100 cycles led to first damping-induced gradual attenuation of maximum stresses till a steady elastic state in the latter cycles (Figure S19, Supporting Information). The excellent elasticity of the ionic elastomer was evidenced from the horizontal stretching tests, which remained at the tensional state (1,000% strain) after several cycles of horizontal stretching (Movie S2, Supporting Information). Stress relaxation experiments determined the relaxation time of the ionic elastomer at 200% tensile strain to be 485 s (Figure S20, Supporting Information), comparable to many biological tissues.[52]

We ascribe the excellent elasticity of PTFEA-*co*-PFOEA ionic elastomer to mainly two origins that play roles at different strain stages. One is the high chain entanglement of PTFEA-rich matrix, which not only allows for large entropic deformation, but also effectively restrains irreversible deformation at low strains. The other origin arises from the strain-enhanced liquid crystal assembly of PFOEA moieties, which can prevent permanent chain sliding at large strains by introducing stronger crosslinks (see illustration in Figure 1b). Such a process was clearly supported by strain-dependent atomic force microscope (AFM) observations. As shown in Figure 4e, apparent phase separation with densely packed sphere-shaped PPFOEA-rich nanophases sized ≈370 nm can be observed at the initial state. Notably, despite the large phase size, the comparable refractive indices between PTFEA-rich matrix and PPFOEA-rich nanophases still led to the macroscopic transparency of ionic elastomer, which was also observed in our recently reported nanomesh-toughened ionic skin.[6] Upon stretching to 200% and 400% strains, the nanophases not only aligned and elongated parallel to the stretching direction, but also grew in size with increasing strains. Further stretching the ionic elastomer to even larger strains would cause the gradual fragmentation of the grown nanophases, as evidenced by AFM and SAXS results (Figure S21, Supporting Information). Nonetheless, the whole stretching process is totally reversible, suggesting that strain-induced nanophase evolution is highly dynamic, which can only be explained by the high deformability and self-assembly characteristic of liquid-like PPFOEA-rich nanophases locating at the rheological dissipating regime. Indeed, by increasing the oscillation strain from 0.1% to 10%, the crossover frequency between rubbery and dissipating regions shifted from 0.35 to 0.18 Hz, corresponding to the extension of the relaxation time related to the Rouse motion of entangled strands (τ_e) and thus enhanced chain association (Figure S22, Supporting Information).

The proposed mechanism of strain-enhanced liquid crystal assembly of PFOEA moieties was also supported by statistical X-ray scattering/diffraction results. As presented in Figure 4f, with increasing strains, the initial power law exponent of −1 at small q regime drastically decreased to −4 at 200% and 400% strains, corresponding to the transformation from a loosely packed disordered structure to a densely packed ordered structure. Moreover, stretching also led to the slight increase of $d_{\text{side-chain}}$ from 0.51 to 0.53 nm (Figure S23, Supporting Information), suggesting that more PFOEA moieties participated in liquid crystal assembly.

Owing to the supramolecular nature and highly dynamic chain association, the PTFEA-*co*-PFOEA ionic elastomer is also self-healable and recyclable even at room temperature, important for stretchable electronics.[53,54] As demonstrated in Figure 4g and Movie S3, Supporting Information, two cut samples stained with Victoria blue B and saffron T dyes, respectively, could heal together in 20 min, and the healed sample can be stretched to 5–8 times its original length. If a small scratch was introduced on the surface of ionic elastomer, only 7 s was needed to heal the damage (Figure S24, Supporting Information). The excellent room-temperature self-healability even allowed powder processing or recycling of the ionic elastomer. For instance, we ground a piece of ionic elastomer into powder with a cryogenic grinder, and then pressed the powder with a mold at 1 MPa for 12 h, and a newly shaped transparent ionic elastomer can be finally obtained (Figure 4h). Moreover, two healed ionic elastomers can be blown into an air-tight balloon (Figure 4i), demonstrating the high quality of self-healing process. Similarly, various shapes of healed ionic elastomer sheets could be obtained with different combinations of tangram pieces (Figure 4j; Figure S25, Supporting Information). We also quantitatively evaluated the self-healing efficiency of ionic elastomer by tensile stress–strain curves. As shown in Figure 4k, the healing efficiency increased with increasing healing time, and after healing for 20 min, the healing efficiency can reach as high as 95% and 86% as evaluated by the restored elongation and toughness, respectively. It is supposed that the excellent self-healability of ionic elastomer should mainly originate from the rapid interchain diffusion within both supramolecular elastic matrix and dissipating nanophases, which is supported by the observation of a recognizable diffusing interlayer between two healed pieces stained by different dyes (Figure S26, Supporting Information).[55,56]

The vibrational energy dissipation-related damping and shock-resistant performance of PTFEA-*co*-PFOEA ionic elastomer was additionally characterized and demonstrated. To comprehensively study the vibration-dependent dynamic behavior of ionic elastomer at different time scales, we plotted the rheological master curves following time-temperature superposition principle at the reference temperature of 20 °C (**Figure 5**a). Similar to typical viscoelastic polymers (Figure 1d), the master curves can be divided into four regimes with increasing frequency, i.e., viscous, rubbery, dissipating, and glassy. The reciprocal of the critical frequency between viscous and rubbery is called the material's whole chain reptation time (τ_{rep}). At frequencies below $1/\tau_{rep}$, the material dissipates

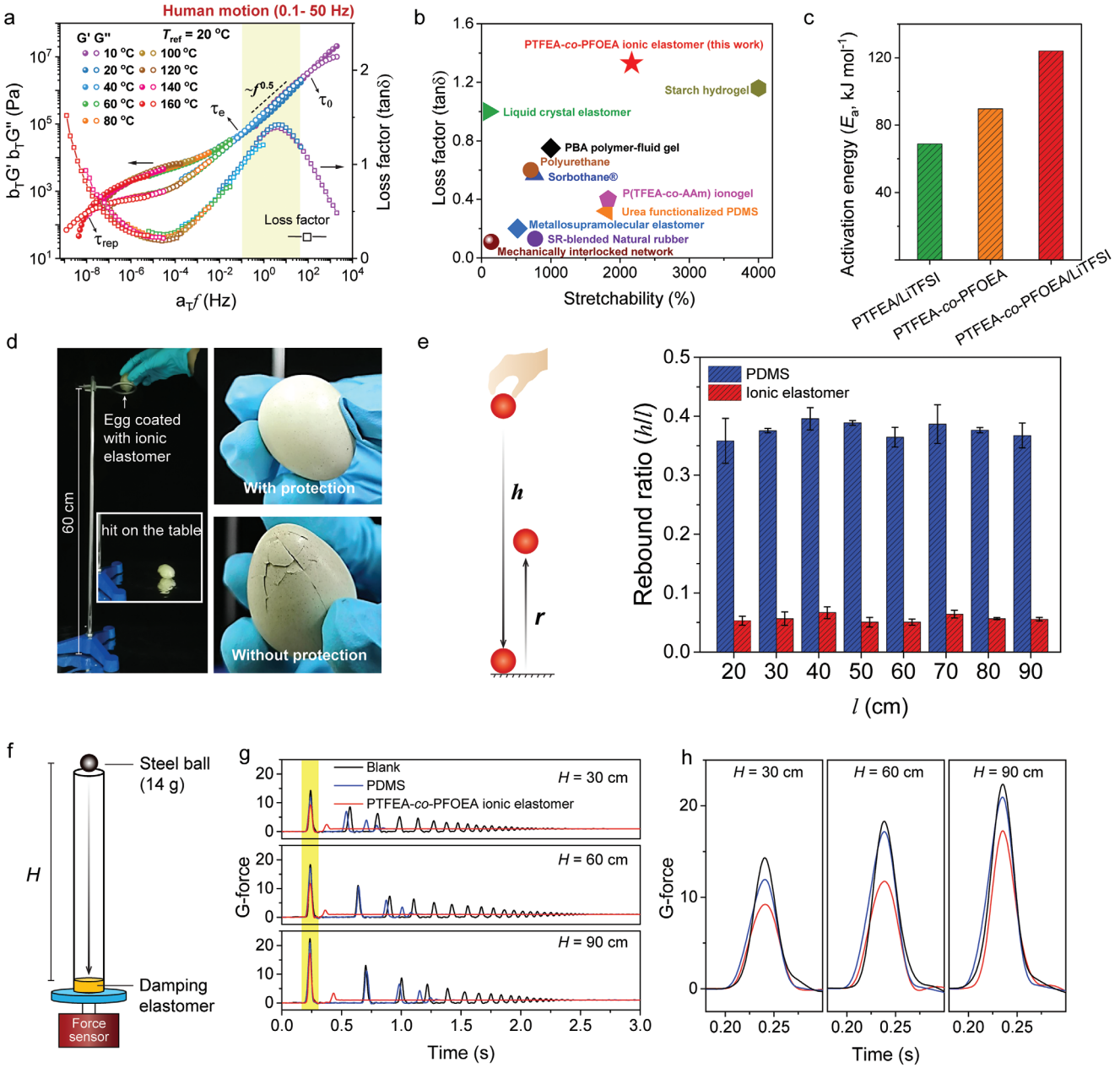

Figure 5. a) Time-temperature superposition rheological and tan δ curves of PTFEA-*co*-PFOEA$_{50\%}$ ionic elastomer at the reference temperature of 20 °C. b) Comparison of the stretchability and loss factor (tan δ at 1 Hz) of the present ionic elastomer with previous damping elastomers/gels. c) Comparison of the activation energies of PTFEA/LiTFSI, PTFEA-*co*-PFOEA, and PTFEA-*co*-PFOEA/LiTFSI. d) Photos of quail eggs wrapped with/without ionic elastomer after falling from a height of 60 cm. e) Rebound ratios of PDMS and ionic elastomer (diameter ≈2 cm) as a function of falling height. The error bars represent ±SD from the mean value (n = 3). f) Schematic experimental set-up for testing shock-controlling performance. g) Time-resolved G-force wave attenuations with the blank sample, PDMS, and ionic elastomer when a 14 g of steel ball fell freely from the height of 30, 60, and 90 cm, respectively. h) Enlarged views of the marked area in (g) for the comparison of the first impulse peak.

more energy than it stores and thus cannot maintain its shape exhibiting fluid-like behavior. The τ_{rep} of ionic elastomer was calculated to be 8.6×10^7 s, extremely long for its excellent shape retention at ambient conditions. The rubbery regime is characterized by an entanglement plateau at the frequencies between $1/\tau_{rep}$ and $1/\tau_e$, where τ_e is the relaxation time related to the Rouse motion of entangled strands (τ_e = 7.4 s for the ionic elastomer). The plateau modulus (G_e) was determined by the minimum tan δ method to be 5.1 kPa (Figure S27, Supporting Information). According to the equation $M_e = \rho RT/G_e$, the number-average molar mass of the entanglement strands (M_e) of ionic elastomer was estimated to be 6.4×10^5 g mol^{-1}, much larger than the minimum possible entanglement molecular weight for polymers ($M_e \approx 10^3$–10^4 g mol^{-1}).[57] At the frequencies between $1/\tau_e$ and $1/\tau_0$ (τ_0 is the Kuhn segment relaxation time; $\tau_0 = 7 \times 10^{-3}$ s for the ionic elastomer), the sticky Rouse

motion of entangled strands is dominant with a typical power-law frequency dependence of the moduli G', $G'' \sim f^{0.5}$.[29] In this dissipating regime, the material becomes liquid-like again with high loss moduli and frictional dynamics. From $\tau_e = \tau_0 N_e^2$, the number of Kuhn segments between entanglement, N_e, was calculated to be as small as 32.4, suggesting easy chain entanglement promoted by stickers.[58] At frequencies larger than $1/\tau_0$, the material enters the glassy state with frozen segmental motions.

It is noteworthy that at the focused human motion frequency range (0.1–50 Hz) in this work, PTFEA-*co*-PFOEA ionic elastomer mainly locates at the dissipating regime dominated by PPFOEA-rich nanophase. That means, molecular frictions are most active in this range contributing to maximum damping capacity. The loss factor, tan δ, is always higher than 1 at this frequency range (20 °C) and reaches a maximum value of 1.4 at 4.6 Hz. To highlight the advantage of the present ionic elastomer in damping performance, we made a rough comparison of the tan δ value at 1 Hz and stretchability with previous damping elastomers and gels. As shown in Figure 5b and Table S2 (Supporting Information), our ionic elastomer ranks in the highest level of damping elastomers with not only superhigh stretchability (2,168%), but also a record-high tan δ value of 1.3 at 1 Hz. It is also noted that at frequencies <0.1 Hz, the ionic elastomer is in the rubbery state dominated by PTFEA-rich elastic matrix, which contributes to the whole material's elasticity at the experimental time scale. We additionally compared the frequency-dependent values of G″ among ionic elastomer, polydimethylsiloxane (PDMS), and D3O (a commercially available polymer damper), which is the measure of the energy dissipated as heat at a specified frequency when the material turns viscous.[46] As shown in Figure S28 (Supporting Information), the ionic elastomer possesses also much higher G″ than PDMS and D3O at the frequencies of 0.1, 1, 10, and 50 Hz, suggesting its better vibrational energy dissipation ability.

We further calculated the activation energies (E_a) of the ionic elastomer with/without PFOEA/LiTFSI from the temperature-dependent horizontal shift factors for superimposed curves (Figure 5c; Figures S29–S31, Supporting Information). The activation energy of PTFEA-*co*-PFOEA/LiTFSI ionic elastomer is ≈124.1 kJ mol^{-1}, much higher than PTFEA/LiTFSI (E_a = 68.8 kJ mol^{-1}) and PTFEA-*co*-PFOEA (E_a = 89.7 kJ mol^{-1}). This again consolidates the roles of both dynamic PFOEA assembly and lithium bonds in the highly dissipating and damping behavior of ionic elastomer.

To demonstrate the damping performance of PTFEA-*co*-PFOEA ionic elastomer, we carried out a few shock-related experiments. We first dropped a quail egg wrapped with/without ionic elastomer on the table from a height of 60 cm (Figure 5d; Movie S4, Supporting Information). Without coating with ionic elastomer, the egg was easily broken caused by the sudden impact force. In contrast, with the protection of ionic elastomer, the egg remained intact, revealing that ionic elastomer is very promising in buffering and absorbing shock energy in the impact events. Rebound is another important property closely related to the energy-dissipating performance. Highly resilient elastomers like PDMS with low energy dissipation have high rebound, and are thus vulnerable to vibration damages, while damping elastomers hardly rebound. We tested the rebound ratios (defined by the ratio of rebound height (r) to dropping (h) height) of PDMS and PTFEA-*co*-PFOEA ionic elastomer for comparison (Figure 5e; Movie S5, Supporting Information). The rebound ratio of ionic elastomer is only 0.05 and almost independent of dropping heights, significantly lower than PDMS ($r/h \approx 0.37$), suggesting again the ionic elastomer's high damping capacity.

We further monitored the G-force changes by the steel ball impact experiments with either PDMS or ionic elastomer protection to compare their shock wave attenuation abilities. As shown in Figure 5f, the high damping performance of ionic elastomer largely reduced the impulse force peaks of the induced shock waves and brought the steel ball quickly to rest, while PDMS showed a poorer damping performance. In the case of dropping the steel ball from the height of 30 cm, the ionic elastomer can reduce the impact force by 36% with the specific damping energy of 11.6 kJ m^{-3} in the first hit, while PDMS reduced the force by only 16% with the specific damping energy of 6.0 kJ m^{-3} (Figure S32, Supporting Information). Increasing dropping heights would reduce the impact force attenuation effect perhaps due to the softness of ionic elastomer with nearly saturated deformation at high impact forces, but the damping energy still increased. The logarithmic decrement (Δ) of the ionic elastomer in the case of 30 cm height was roughly estimated to be 1.31 ($\Delta = \ln(F_n/F_{n+1})$; F_n is the peak force of the nth vibration),[46] much higher than that of PDMS (Δ = 0.54), again highlighting the superb damping capacity of ionic elastomer.

The ionic elastomer also presents excellent damping capacity with continuous vibration stimulation. An apparent damping-induced hysteresis between oscillation force and strain curves in the compressive mode was observed for ionic elastomer at both the frequencies of 0.1 and 1 Hz, while PDMS showed almost no hysteresis (Figure S33, Supporting Information). In addition, continuously pressing the ionic elastomer to 50% strain at the frequency of 0.5 Hz led to a significant decay of maximum force, while purely elastic PDMS maintained a steady force level (Figure S34, Supporting Information). All the above results clearly show that the high damping capacity of ionic elastomer with great deceleration and force attenuation effect may afford excellent protection for the electronic elements beneath from shock-related vibration damages.

As the candidate ionic skin for soft electronics and robotics, the sensing performance of PTFEA-*co*-PFOEA ionic elastomer was finally investigated. By coating the ionic elastomer with a thin dielectric perfluoroether elastomer layer, the material can be used for self-powered sensing based on the single-electrode-mode triboelectric mechanism (Figure S35, Supporting Information). Similar to many other stretchable ionic conductor-based triboelectric sensors,[59] the present ionic elastomer-based sensor exhibited reliable voltage signal feedback by varying touched materials, frequencies, and pressing forces (Figures S36–S38, Supporting Information).

3. Conclusion

In summary, we here present a highly damping and self-healable ionic elastomer from the polymerization-induced dynamic phase separation of sticky fluorinated copolymers. The ionic elastomer

features an adipose tissue-like two-phase structure with highly dissipating long-side-chain PPFOEA-rich nanophases embedded in an elastic short-side-chain PTFEA-rich matrix, wherein rigid PFOEA moieties tend to form transient liquid crystal assemblies contributing to strong molecular frictions. Such a unique material design defeats the long-term conflict among damping, elasticity, and self-healability as encountered by conventional ionic skins. By balancing chain entanglement and associating dynamics, the optimal ionic elastomer with equimolar TFEA and PFOEA demonstrates a few fascinating properties including high stretchability, softness, strain-adaptive stiffening, good elastic recovery, room temperature self-healability, and powder-based recyclability. More intriguingly, the ionic elastomer shows ultrahigh loss factors ($\tan \delta > 1$) at the comparable frequencies to human motions (0.1–50 Hz), which can be potentially used in shock-resistant damping applications as protective ionic skins for bionic soft robots and machines. This biomimetic design can be easily extended to other sticky polymer systems to produce highly robust ionic skins with global resistances to various damages like natural skins.

Supporting Information

Supporting Information is available from the Wiley Online Library or from the author.

Acknowledgements

The authors appreciate the supports from the National Natural Science Foundation of China (NSFC) (nos. 21991123, 22275032, 52161135102, and 51873035). The authors also thank the staff from BL16B beamline at Shanghai Synchrotron Radiation Facility (SSRF) for assistance during data collection.

Conflict of Interest

The authors declare no conflict of interest.

Data Availability Statement

The data that support the findings of this study are available from the corresponding author upon reasonable request.

Keywords

damping, elastomers, ionic skins, phase separation, self-healable

[1] Z. Lei, P. Wu, *Acc Mater. Res.* **2021**, *2*, 1203.
[2] C. Y. Wang, H. Y. Wang, B. H. Wang, H. Miyata, Y. Wang, M. O. G. Nayeem, J. J. Kim, S. Lee, T. Yokota, H. Onodera, T. Someya, *Sci. Adv.* **2022**, *8*, eabo1396.
[3] K. Park, H. Yuk, M. Yang, J. Cho, H. Lee, J. Kim, *Sci. Robot.* **2022**, *7*, eabm7187.
[4] Z. Wang, J. Wang, J. Ayarza, T. Steeves, Z. Hu, S. Manna, A. P. Esser-Kahn, *Nat. Mater.* **2021**, *20*, 869.
[5] B. Park, J. H. Shin, J. Ok, S. Park, W. Jung, C. Jeong, S. Choy, Y. J. Jo, T. I. Kim, *Science* **2022**, *376*, 624.
[6] J. Wang, B. Wu, P. Wei, S. Sun, P. Wu, *Nat. Commun.* **2022**, *13*, 4411.
[7] W. Li, L. Li, S. Zheng, Z. Liu, X. Zou, Z. Sun, J. Guo, F. Yan, *Adv. Mater.* **2022**, *34*, 2203049.
[8] W. Zhang, B. Wu, S. Sun, P. Wu, *Nat. Commun.* **2021**, *12*, 4082.
[9] T. Li, Y. Wang, S. Li, X. Liu, J. Sun, *Adv. Mater.* **2020**, *32*, 2002706.
[10] A. A. Gusev, K. Feldman, O. Guseva, *Macromolecules* **2010**, *43*, 2638.
[11] D. Ratna, B. C. Chakraborty in *Polymers for Vibration Damping Applications*, Elsevier, Amsterdam, Netherlands **2020**.
[12] J. Huang, Y. C. Xu, S. H. Qi, J. J. Zhou, W. Shi, T. Y. Zhao, M. J. Liu, *Nat. Commun.* **2021**, *12*, 3610.
[13] K. Urayama, T. Miki, T. Takigawa, S. Kobjiya, *Chem. Mater.* **2004**, *16*, 173.
[14] X. Lin, Y. Liu, A. Bai, H. Cai, Y. Bai, W. Jiang, H. Yang, X. Wang, L. Yang, N. Sun, H. Gao, *Nat. Biomed. Eng.* **2019**, *3*, 632.
[15] Y. J. Wang, Y. He, S. Y. Zheng, Z. Y. Xu, J. Li, Y. P. Zhao, L. Chen, W. G. Liu, *Adv. Funct. Mater.* **2021**, *31*, 2104296.
[16] Z. Y. Lei, P. Y. Wu, *Nat. Commun.* **2019**, *10*, 3429.
[17] F. Faghihi, N. Mohammadi, P. Hazendonk, *Macromolecules* **2011**, *44*, 2154.
[18] W. C. Wang, D. T. Zhao, J. N. Yang, T. Nishi, K. Ito, X. Y. Zhao, L. Q. Zhang, *Sci. Rep.* **2016**, *6*, 22810.
[19] E. Croisier, S. Liang, T. Schweizer, S. Balog, M. Mionic, R. Snellings, J. Cugnoni, V. Michaud, H. Frauenrath, *Nat. Commun.* **2014**, *5*, 4728.
[20] S. Ganesh, S. N. Subraveti, S. R. Raghavan, *ACS Appl. Mater. Interfaces* **2022**, *14*, 20014.
[21] S. A. Cazzell, B. Duncan, R. Kingsborough, N. Holten-Andersen, *Adv. Funct. Mater.* **2021**, *31*, 2009118.
[22] D. Zhao, Z. M. Zhang, J. Zhao, K. Liu, Y. H. Liu, G. F. Li, X. H. Zhang, R. X. Bai, X. Yang, X. Z. Yan, *Angew. Chem., Int. Ed.* **2021**, *60*, 16224.
[23] H. Yamazaki, M. Takeda, Y. Kohno, H. Ando, K. Urayama, T. Takigawa, *Macromolecules* **2011**, *44*, 8829.
[24] M. O. Saed, W. Elmadih, A. Terentjev, D. Chronopoulos, D. Williamson, E. M. Terentjev, *Nat. Commun.* **2021**, *12*, 6676.
[25] A. Pissarenko, M. A. Meyers, *Prog. Mater. Sci.* **2020**, *110*, 100634.
[26] A. S. G. van Oosten, X. Y. Chen, L. K. Chin, K. Cruz, A. E. Patteson, K. Pogoda, V. B. Shenoy, P. A. Janmey, *Nature* **2019**, *573*, 96.
[27] M. Geerligs, G. W. M. Peters, P. A. J. Ackermans, C. W. J. Oomens, F. P. T. Baaijens, *Biorheology* **2008**, *45*, 677.
[28] K. Comley, N. A. Fleck, *Int. J. Solids Struct.* **2010**, *47*, 2982.
[29] M. Rubinstein, A. N. Semenov, *Macromolecules* **2001**, *34*, 1058.
[30] K. Honda, M. Morita, H. Otsuka, A. Takahara, *Macromolecules* **2005**, *38*, 5699.
[31] W. W. Niu, G. Y. Chen, H. L. Xu, X. K. Liu, J. Q. Sun, *Adv. Mater.* **2022**, *34*, 2108232.
[32] Z. T. Chen, K. K. S. Lau, *Macromolecules* **2019**, *52*, 5183.
[33] C. Ranacher, R. Resel, P. Moni, B. Cermenek, V. Hacker, A. M. Coclite, *Macromolecules* **2015**, *48*, 6177.
[34] M. X. Li, L. L. Chen, Y. R. Li, X. B. Dai, Z. K. Jin, Y. C. Zhang, W. W. Feng, L. T. Yan, Y. Cao, C. Wang, *Nat. Commun.* **2022**, *13*, 2279.
[35] M. X. Wang, P. Y. Zhang, M. Shamsi, J. L. Thelen, W. Qian, V. K. Truong, J. Ma, J. Hu, M. D. Dickey, *Nat. Mater.* **2022**, *21*, 359.
[36] Y. M. Kim, H. C. Moon, *Adv Funct Mater* **2020**, *30*, 1907290.
[37] L. H. Sperling in *Introduction to Physical Polymer Science*, John Wiley & Sons, NY, USA **2005**.

[38] P. Shi, Y. Wang, K. Wan, C. Zhang, T. Liu, *Adv. Funct. Mater.* **2022**, *32*, 2112293.
[39] L. G. Xu, Z. K. Huang, Z. S. Deng, Z. K. Du, T. L. Sun, Z. H. Guo, K. Yue, *Adv. Mater.* **2021**, *33*, 2105306.
[40] J. Chen, Y. Y. Gao, L. Shi, W. Yu, Z. J. Sun, Y. F. Zhou, S. Liu, H. Mao, D. Y. Zhang, T. Q. Lu, Q. Chen, D. M. Yu, S. J. Ding, *Nat. Commun.* **2022**, *13*, 4868.
[41] X. H. Meng, Y. Qiao, C. Do, W. Bras, C. Y. He, Y. B. Ke, T. P. Russell, D. Qiu, *Adv. Mater.* **2022**, *34*, 2108243.
[42] Y. J. Wang, S. T. Sun, P. Y. Wu, *Adv. Funct. Mater.* **2021**, *31*, 2101494.
[43] X. Chen, Y. K. Bai, C. Z. Zhao, X. Shen, Q. Zhang, *Angew. Chem., Int. Ed.* **2020**, *59*, 11192.
[44] B. R. B. Yiming, Y. Han, Z. L. Han, X. N. Zhang, Y. Li, W. Z. Lian, M. Q. Zhang, J. Yin, T. L. Sun, Z. L. Wu, T. F. Li, J. Z. Fu, Z. Jia, S. X. Qu, *Adv. Mater.* **2021**, *33*, 2006111.
[45] X. Yao, S. S. Dunn, P. Kim, M. Duffy, J. Alvarenga, J. Aizenberg, *Angew. Chem., Int. Ed.* **2014**, *53*, 4418.
[46] R. D. Corsaro, L. H. Sperling in *Sound and Vibration Damping with Polymers*, American Chemical Society, Washington DC **1990**.
[47] D. H. C. Wong, J. L. Thelen, Y. B. Fu, D. Devaux, A. A. Pandya, V. S. Battaglia, N. P. Balsara, J. M. DeSimone, *Proc. Natl. Acad. Sci. USA.* **2014**, *111*, 3327.
[48] X. E. Wang, C. Zhang, M. Sawczyk, Q. H. Yuan, F. F. Chen, T. C. Mendes, P. C. Howlett, C. K. Fu, P. Kral, C. J. Hawker, A. Whittaker, M. Forsyth, J. Sun, Y. Q. Wang, X. Tan, D. J. Searles, *Nat. Mater.* **2022**, *21*, 1057.
[49] S. T. Sun, P. Y. Wu, *Chin. J. Polym. Sci.* **2017**, *35*, 700.
[50] C. Q. Luo, C. Chung, N. A. Traugutt, C. M. Yakacki, K. N. Long, K. Yu, *ACS Appl. Mater. Interfaces* **2021**, *13*, 12698.
[51] https://www.sorbothane.com/impact-of-shock-absorption.aspx (accessed: March 2017).
[52] O. Chaudhuri, J. Cooper-White, P. A. Janmey, D. J. Mooney, V. B. Shenoy, *Nature* **2020**, *584*, 535.
[53] C. Shi, Z. Zou, Z. Lei, P. Zhu, W. Zhang, J. Xiao, *Sci. Adv.* **2020**, *6*, eabd0202.
[54] C. Q. Shi, Z. N. Zou, Z. P. Lei, P. C. Zhu, G. H. Nie, W. Zhang, J. L. Xiao, *Research* **2021**, *14*, 9846036.
[55] S. Wang, M. W. Urban, *Nat. Rev. Mater.* **2020**, *5*, 562.
[56] M. Hai, Q. Zhang, Z. Li, M. Cheng, A. J. C. Kuehne, F. Shi, *Supramol. Mater.* **2022**, *1*, 100009.
[57] W. F. M. Daniel, J. Burdynska, M. Vatankhah-Varnoosfaderani, K. Matyjaszewski, J. Paturej, M. Rubinstein, A. V. Dobrynin, S. S. Sheiko, *Nat. Mater.* **2016**, *15*, 183.
[58] L. Chen, T. L. Sun, K. P. Cui, D. R. King, T. Kurokawa, Y. Saruwatari, J. P. Gong, *J Mater Chem* **2019**, *7*, 17334.
[59] Y. H. Wu, Y. Luo, T. J. Cuthbert, A. V. Shokurov, P. K. Chu, S. P. Feng, C. Menon, *Adv. Sci.* **2022**, *9*, 2106008.